

pubs.acs.org/NanoLett Letter

Probing the Melting Transitions in Phase-Change Superlattices via Thin Film Nanocalorimetry

Jie Zhao, [∇] Asir Intisar Khan, [∇] Mikhail Y. Efremov, Zichao Ye, Xiangjin Wu, Kangsik Kim, Zonghoon Lee, H.-S. Philip Wong, Eric Pop, and Leslie H. Allen*



Cite This: Nano Lett. 2023, 23, 4587-4594



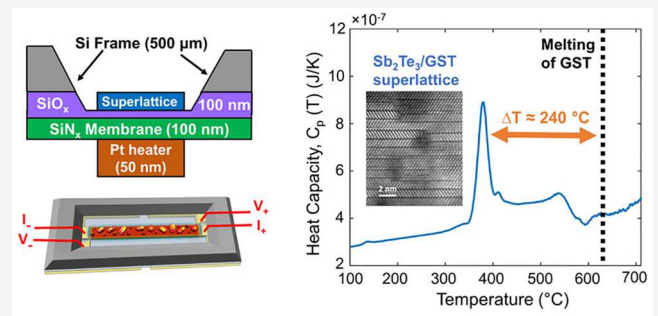
ACCESS

III Metrics & More

Article Recommendations

s Supporting Information

ABSTRACT: Phase-change superlattices with nanometer thin sublayers are promising for low-power phase-change memory (PCM) on rigid and flexible platforms. However, the thermodynamics of the phase transition in such nanoscale superlattices remain unexplored, especially at ultrafast scanning rates, which is crucial for our fundamental understanding of superlattice-based PCM. Here, we probe the phase transition of Sb₂Te₃ (ST)/Ge₂Sb₂Te₅ (GST) superlattices using nanocalorimetry with a monolayer sensitivity (\sim 1 Å) and a fast scanning rate (10^5 K/s). For a 2/1.8 nm/nm Sb₂Te₃/GST superlattice, we observe an endothermic melting transition with an \sim 240 °C decrease in temperature and an \sim 8-fold decrease in enthalpy compared to those for the melting of GST, providing key thermodynamic



Nanocalorimetry of Phase-Change Superlattices

insights into the low-power switching of superlattice-based PCM. Nanocalorimetry measurements for Sb₂Te₃ alone demonstrate an intrinsic premelting similar to the unique phase transition of superlattices, thus revealing a critical role of the Sb₂Te₃ sublayer within our superlattices. These results advance our understanding of superlattices for energy-efficient data storage and computing.

KEYWORDS: phase-change superlattice, nanocalorimetry, phase transition, melting enthalpy, superlattice interface, ultrafast scanning

Phase-change memory (PCM) stores data in two material phases, glassy and crystalline, that have different electrical conductances. PCM is a prospective memory technology given its unique characteristics of nonvolatility, a short read/write time, high endurance, and insusceptibility to ionizing radiation. A continuous change in the conductance states of PCM resembles the behavior of synapses and may be used to realize brain-inspired computing networks. PCM devices based on chalcogenide materials such as $Ge_2Sb_2Te_5$ (GST) undergo a reversible phase transition between crystalline (low-resistance state) and melt-quenched amorphous (high-resistance state) phases. These transitions are induced by Joule heating using nanosecond electrical pulses, which, however, require a large switching current, and remain a concern for traditional PCM devices.

Recently, significant progress has been reported to decrease the switching current of PCM via a superlattice (SL) platform with alternating sublayers of phase-change materials such as ${\rm Sb_2Te_3/Ge_2Sb_2Te_5}$ (ST/GST), ${\rm GeTe/Sb_2Te_3}$, ${\rm II-II}$ and ${\rm TiTe_2/Sb_2Te_3}$. Simple epitaxial layering of these chalcogenides into a superlattice-like stack triggers a dramatic change in the transformation of the materials, i.e., switching of their phases. The reason for this effect is still not yet well-understood. One hypothesis proposed that a crystalline-to-crystalline phase transition (resistance change via subtle

movement of Ge atoms), (instead of a melt—quench transition in conventional PCMs) triggers a decrease in the switching current in the GeTe/Sb₂Te₃ SL. ^{11,15} More recently, studies found that van der Waals (vdW) interfaces within SLs are responsible for the increased out-of-plane thermal resistance and the unique anisotropy of thermal and electrical conductivity, facilitating the low-power switching in PCM devices. ^{16–19} However, the nature of the phase transition in the SL and its corresponding thermodynamic metrics (e.g., temperature, enthalpy, and entropy) remain unexplored, especially under conditions close to those of actual PCM device operation (thin film format and fast scanning rates).

Here, we report the phase transition of phase-change ST/GST SLs (65 nm thick) for the first time using thin film nanocalorimetry (NanoDSC).^{20–25} SL samples are directly sputtered on the NanoDSC sensors without additional destructive preparations which are otherwise required for conventional calorimetry. The monolayer sensitivity (~1 Å) of

 Received:
 March 19, 2023

 Revised:
 May 10, 2023

 Published:
 May 12, 2023





Nano Letters pubs.acs.org/NanoLett Letter

our NanoDSC enables superlattice materials probing of the same form (\sim 60 nm thin film) as that in actual PCM devices, while its ultrafast scanning rate (10^5 K/s) captures metastable transitions in a time frame close to that of the device switching. Multiple thermodynamic fingerprints are uncovered, including a sharp endothermic transition at \sim 380 °C for a 2/1.8 nm/nm ST/GST SL, which provides seminal clues about the lowenergy consumption and increased endurance characteristics of SL-based PCMs. This transition is \sim 240 °C lower than the melting (\sim 620 °C) of bulk GST, along with an 8-fold decrease in the transition enthalpy.

Table I summarizes the names and descriptions of all of the samples in this work. They are either ST/GST SLs or

Table I. Names and Descriptions of Samples Used in This Work

sample	description of the sample
2-SL-A	2/1.8 nm/nm ST/GST superlattice (65 nm thick)
16-SL-A	(first) 16/14.4 nm/nm ST/GST superlattice (65 nm thick)
16-SL-B	(second) 16/14.4 nm/nm ST/GST superlattice (65 nm thick)
ST-A	32 nm thick ST deposited on a 4 nm ST seed layer
GST-A	28.8 nm thick GST deposited on a 4 nm ST seed layer

homogeneous ST and GST films sputtered on a SiN_x/SiO_x membrane of NanoDSC sensors (Figure 1a,b) using a self-aligned shadow mask.²⁷ Sensors are attached on a Si wafer using Kapton tape during the sample depositions. Samples are sputtered using the same deposition recipe as the one used to fabricate the SL-based PCM devices (described elsewhere).^{10,13} Sputtering starts with a 4 nm thick seed ST layer at room temperature (RT), followed by the deposition of

subsequent GST/ST layers at 180 $^{\circ}$ C. This procedure ensures that all of the GST sublayers have a face-centered cubic (FCC) crystal structure. Similar to PCM devices, a 10 nm thick TiN capping layer is sputtered at RT to minimize oxidation and evaporation of SLs during the high-temperature NanoDSC scans.

SL stacking of the sputtered samples is verified by STEM imaging. Figure 1c reveals the atomically sharp interlayer vdW gaps inherent in the 2/1.8 nm/nm ST/GST SL deposited on a Si substrate with native SiO_x . Schematic of a 2/1.8 nm/nm ST/GST SL is also shown in Figure 1d (same as 2-SL-A on a sensor). The vdW gaps are intrinsic to the ST sublayer as they also occur in bulk ST.

Differential mode NanoDSC measurements are performed in vacuum (2×10^{-7} Torr) for a series of temperature ramping from RT to the maximum temperature ($T_{\rm max}$) with a heating rate of (1.1 ± 0.1) × 10^5 K/s. A series consists of either a single scan or multiple scans with 1 s intervals, which are sufficient to passively cool samples to RT. Here, we denote each calorimetry scan as "sample ID- N_1 - N_2 ", where N_1 is the pulse series name and N_2 is the scan number in a specific pulse series. All scans in this work are summarized in section I of the Supporting Information (SI). NanoDSC has recently revealed excellent quantitative consistency and accuracy in the measurement of the transition temperature and enthalpy for a 20 nm thick GST film upon various heating rates. ²⁸ Operation and data analysis were further detailed in our previous works. ^{22,23}

Calorimetric results of all samples show complicated phase transition fingerprints that are sensitive to scanning history. Their metastability presents challenges to calorimetry measure-

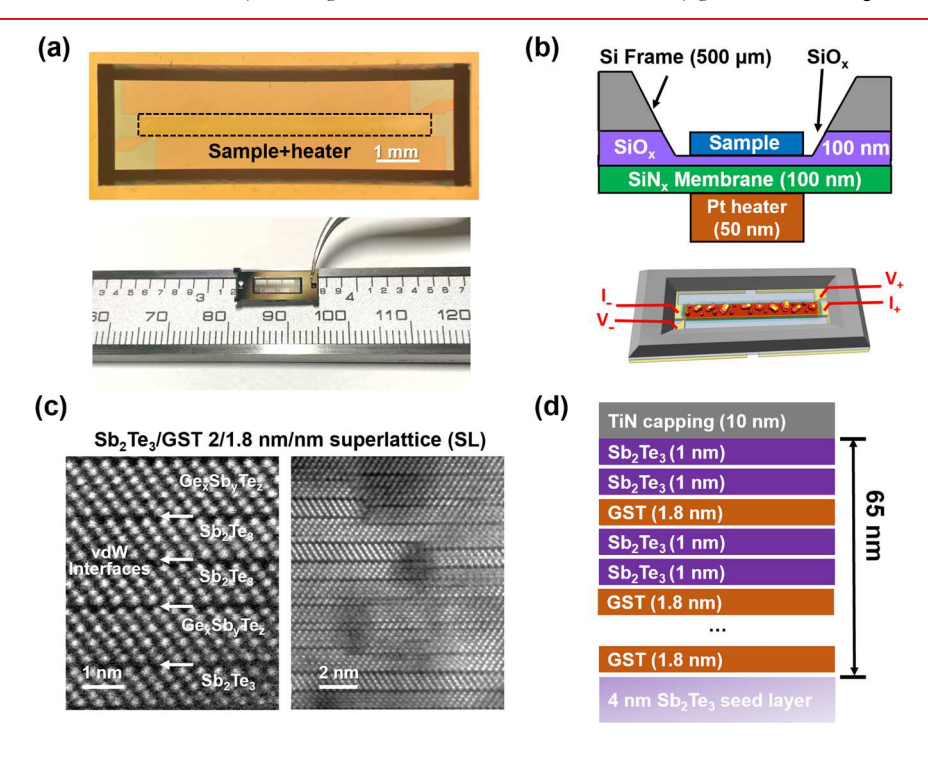


Figure 1. NanoDSC characterization of $Sb_2Te_3/Ge_2Sb_2Te_5$ (ST/GST) superlattices. (a) Optical image of a NanoDSC sensor. A caliper scale is shown for comparison. (b) Schematic of a NanoDSC sensor, including the deposited ST/GST superlattice sample (dimension not shown to scale). Reproduced with permission from ref 26. Copyright 2009 American Chemical Society. (c) High-angle annular dark-field scanning transmission electron microscopy (STEM) cross sections of the as-deposited 2/1.8 nm/nm ST/GST superlattice that shows atomically sharp vdW interfaces as well as defects such as planar grain boundaries and triple junctions, which extend across several sublayers. (d) Schematic of a 65 nm thick 2/1.8 nm/nm ST/GST superlattice stack with alternating double-layer Sb_2Te_3 and single-layer $Ge_2Sb_2Te_5$.

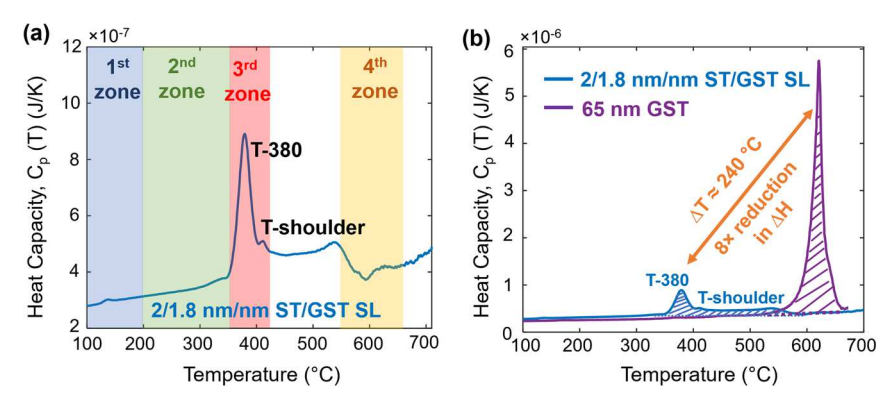


Figure 2. (a) $C_p(T)$ profile of scan 2-SL-A-6-1 (2/1.8 nm/nm ST/GST superlattice). It demonstrates a sharp endothermic transition at 380 °C (T-380) followed by a shoulder (T-shoulder) up to 560 °C, whereas minimal bulk melting signals of ST or GST are observed at ~600 °C. $^{28-31}$ Shaded regimes denote the four temperature zones discussed in this work. (b) Comparison of $C_p(T)$ profiles between the scan in panel a and that of 65 nm thick GST (equivalent to the total thickness of the SL, rescaled from 20 nm thick homogeneous GST sputtered at RT with no ST seed layer). The 65 nm GST melts at 620 °C. The T-380 peak in the superlattice (blue shaded peak) demonstrates an ~240 °C decrease in peak temperature (T_m = 380 °C) and an 8-fold decrease in the transition enthalpy (ΔH_m = 15 μ J for T-380), compared to that during the melting of GST (purple shaded peak). The overall enthalpy in SL (T-380 peak and T-shoulder; ΔH_m = 35 μ J) is also 4-fold smaller than that of GST.

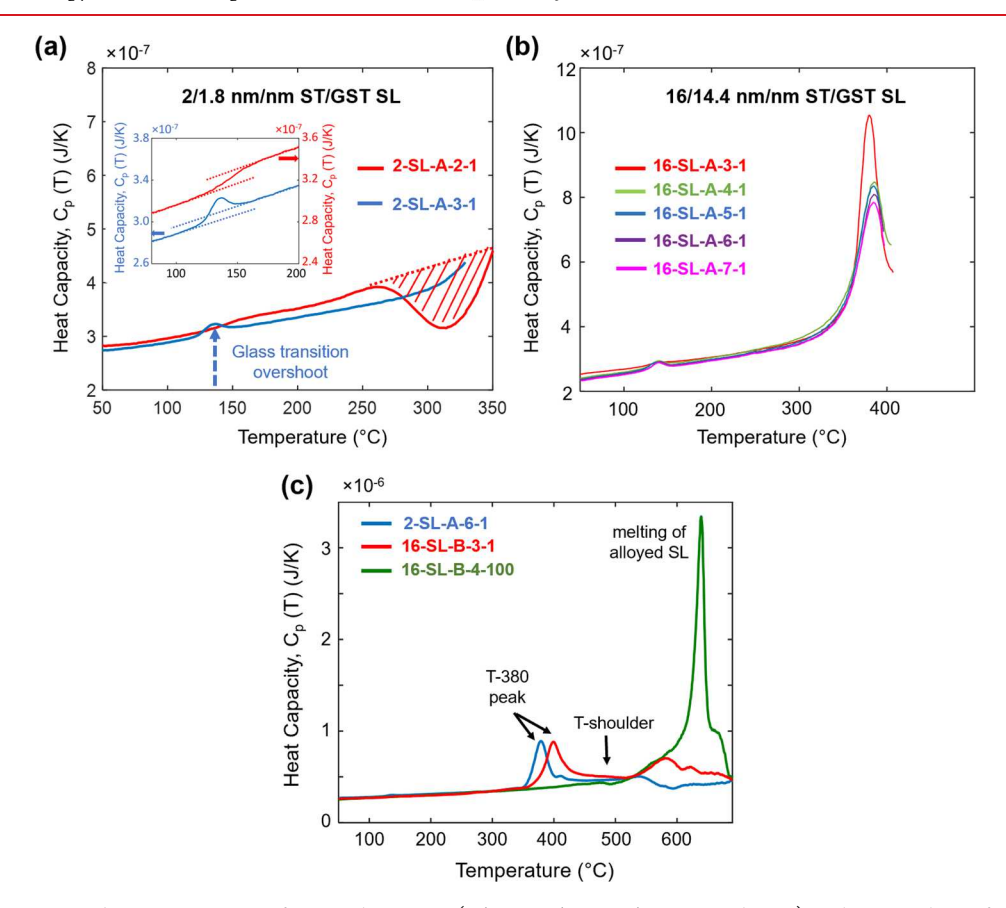


Figure 3. (a) 2-SL-A-2-1 and 2-SL-A-3-1 scans for sample 2-SL-A (2/1.8 nm/nm ST/GST superlattice) with $T_{\rm max}$ values of <350 °C. The inset shows the glass transition features in both curves with 80 °C < T < 200 °C. (b) $C_p(T)$ of 16-SL-A- N_1 -1 (N_1 = 1-6) for a 16/14.4 nm/nm ST/GST superlattice with $T_{\rm max}$ values of <410 °C. (c) First $C_p(T)$ scan to 710 °C for a 16/14.4 nm/nm ST/GST superlattice (16-SL-B-3-1, red curve) and a 2/1.8 nm/nm ST/GST superlattice (2-SL-A-6-1, blue curve). After electrical annealing to 710 °C (100 pulses), a 16/14.4 nm/nm ST/GST stack (2-SL-B-4-100, green curve) shows a melting peak at 630 °C with no T-380 transition. The green curve is rescaled to compensate for the 20% decrease in heat capacity (loss of sample due to evaporation) during electrical annealing.

ments, because heating scans may simultaneously anneal and change the sample. On one hand, NanoDSC with fast scanning rate can capture the metastable transitions of SL and is key to understanding the switching of PCM devices. On the other hand, metastability introduces complexity to the scanning schedule for reliable results.

The calorimetry profile of "conditioned" 2-SL-A-6-1 (with prescans as defined below) up to 710 °C is shown in Figure 2a. A sharp endothermic melting transition at \sim 380 °C (T-380), followed by a shoulder pattern (T-shoulder), is observed, with minimal signs of bulk melting of the constituent ST or GST sublayers of the SL (here 2/1.8 nm/nm ST/GST). This is

Nano Letters pubs.acs.org/NanoLett Letter

unexpected because the phase diagram of bulk ST-GST predicts a melting at ${\sim}600~^{\circ}\mathrm{C}.^{28-31}$ The T-shoulder resembles the calorimetry profile of binary systems with incongruently melting compounds. The term "conditioned" here means the as-deposited SL has undergone a selected series of calorimetry scans ($T_{\text{max}}=200-350~^{\circ}\mathrm{C}$) beforehand. As-deposited SL-based PCM devices also require ${\sim}1000$ low-power cycles for their stable repeated switching. 10

The T-380 transition, which we identify as mainly a crystalline-to-liquid melting transition (see section II of the Supporting Information for justifications), is the most consequential finding in this paper. It provides insight into the crystalline-to-amorphous switching transition in SL-based PCM with an 8-fold lower switching power, compared to those of conventional PCM devices. 10 Calorimetry profiles of 2-SL-A-6-1 and standard GST samples (RT sputtered) are shown in Figure 2b. An ~240 °C decrease in the melting temperature $(T_{\rm m})$ and an 8-fold decrease in transition enthalpy $(\Delta H_{\rm m})$ are observed. The reduced enthalpy of the T-380 transition is expected from Hess' analysis^{33°} as a consequence of the low transition temperature (see section III of the Supporting Information). However, the reduced $T_{\rm m}$ cannot be explained by the phase diagram given the similar composition of Te (GST, 56% Te; SL, 58% Te).

Apart from T-380, a series of other transition features have been identified for a SL. They provide valuable insight into the possible presence of metastable phases (e.g., Te-rich phases) that can greatly reduce the $T_{\rm m}$ of SLs and provide further insight into the T-380 transition as we will explore below. We partition this discussion into the following four temperature zones (Figure 2a): (1) T < 200 °C, (2) 200 °C < T < 350 °C, (3) 350 °C < T < 420 °C, and (4) T > 550 °C.

The first temperature zone (T < 200 °C) demonstrates a glass transition ("T-glass") that shows negligible changes under multiple scans with $T_{\rm max}$ values of <180 °C. This is expected given that our SLs are deposited at 180 °C. For all 65 nm SL samples in this study, the measured heat capacity $C_p(100$ °C) of 279 \pm 8 nJ/K agrees with the calculation (detailed in section IV of the Supporting Information).

The glass transition is observed for all SLs in this study, with a similar glass transition temperature ($T_{\rm g}=140\pm5~{\rm ^{\circ}C}$) at the first scan up to $T_{\rm max}$ values of <200 ${\rm ^{\circ}C}$, indicating a small amount of glassy phase in the as-deposited SLs. $T_{\rm g}$ is assigned from the limiting fictive temperature analysis. For example, scan 2-SL-A-2-1 (Figure 3a, red curve) demonstrates a step-like feature that resembles a "normal" glass transition with a $T_{\rm g}$ of 142 ${\rm ^{\circ}C}$.

The low value of $T_{\rm g}$ deserves to be discussed further. Multiple glass phases are known for the Ge–Sb–Te system. However, a $T_{\rm g}$ of <140 °C is found only in Te-rich phases [atomic composition of Te of >85% (see section V of the Supporting Information)]. It leads to the assumption that Terich phases may be responsible for the observed glass transitions in the SL samples under investigation.

Because the step height of the T-glass ($\Delta C_p = C_{p\text{-liquid}} - C_{p\text{-amorphous}}$ at $T = T_{\rm g}$) is proportional to the amount of the glassy phase, the quantity of the glassy Te-rich compounds can be estimated using the specific/reference ΔC_p reported for ${\rm Ge_{15}Te_{85}}$ glass. For instance, scan 2-SL-A-2-1 shows $\Delta C_p = 15 \pm 1$ nJ/K and thus $6 \pm 0.4\%$ of the film is glassy (detailed in section V of the Supporting Information). Such a small amount of glass agrees with the STEM observation (Figure 1c) that the as-deposited SL is mostly crystalline. It should be noted that

even with the existence of 6% Te-rich glassy phases, the overall stoichiometry for the rest of the SL remains approximately the same (Te \sim 56%) with only 2% deviations.

With regard to the second temperature zone (200 °C < T < 350 °C), a broad exothermic feature (denoted as T-exo) with a $\Delta H_{\rm exo}$ of 5.5 μ J spanning from 250 to 350 °C is observed for 2-SL-A [scan 2-SL-A-2-1 (red curve in Figure 3a)]. This transition is irreversible because it can be observed only on the very first scan to 350 °C. From scan 2-SL-A-2-1 to the subsequent 2-SL-A-3-1 scan (red and blue curves in Figure 3a), we find the $T_{\rm g}$ of 2-SL-A shifts from 142 to 95 °C with a strong "overshoot" and the corresponding amount of glass decreases from 6% to 3% (detailed in section V of the Supporting Information).

It is reasonable to assume that the Te-rich liquid phases formed from the glass transition of the prior scan (e.g., 2-SL-A-2-1) are partially crystallized at the increased temperature, yielding the exothermic transition. This crystallization results in the smaller amount of Te-rich glass observed in the following scan (e.g., 2-SL-A-3-1). However, such a mechanism does not fully explain the strength of T-exo. $\Delta H_{\rm exo}$ estimated solely from the reduction of Te-rich glass (3%) is only 2.0 μJ [assuming the glassy phase is $Ge_{15}Te_{85}^{35}$ (detailed in section V of the Supporting Information)], which is 3-fold lower than the measured $\Delta H_{\rm exo}$. Thus, other exothermic processes may also contribute, including the FCC to hexagonal transition, mixing, and structural relaxation.

The glass transition also developed an "overshoot" feature in scan 2-SL-A-3-1 that is demonstrated by glasses with a specific thermal history, e.g., when the cooling rate during the glass formation is lower than the heating rate of the following calorimetric scan. This condition is typical for adiabatic NanoDSC (see section VI of the Supporting Information for a discussion of the "overshoot").

The third temperature zone (350 °C < T < 420 °C) displays the key finding of the work. The endothermic T-380 transition (as discussed above), shows up in all SL samples. With 16-SL-A as an example, its T-380 melting transition (red curve in Figure 3b) is obtained from a scan up to a $T_{\rm max}$ of ~410 °C after multiple low-temperature prepulses to a $T_{\rm max}$ of 260 °C. Subsequent scans with $T_{\rm max}$ values of <410 °C demonstrate excellent repeatability of the transition with a <1% loss of peak height on average. We speculate that such a reproducible transition is responsible for triggering the electrical switching in ST/GST SL-based PCM devices. From a thermal budget perspective, a single scan (30 ms heating and cooling cycle) in NanoDSC is equivalent to ~10^6 × 30 ns pulses (i.e., ~10^6 switching cycles) in PCM devices.

Te-rich compounds are the only material species that show melting at ~380 °C based on the Ge–Sb–Te phase diagram. Therefore, from a calorimetry perspective, the crystalline Terich phases formed during the "conditioning" of SL may be a critical factor to the T-380 transition. However, they cannot be the main contributor to the T-380 transition enthalpy due to their small amount. Assuming the $Ge_{15}Te_{85}$ mentioned above as the Te-rich compound within our SL, the calculated melting enthalpy of crystalline Te-rich phases is only 2.6 μ J compared to the T-380 transition enthalpy ($\Delta H_{\rm m} = 15$ –20 μ J) measured in this work (see section V of the Supporting Information). Therefore, the T-380 endothermic transition may be associated with the melting of other metastable phases not in the phase diagram. We note that both the T-380 transition and the exothermic crystallization have also been previously observed

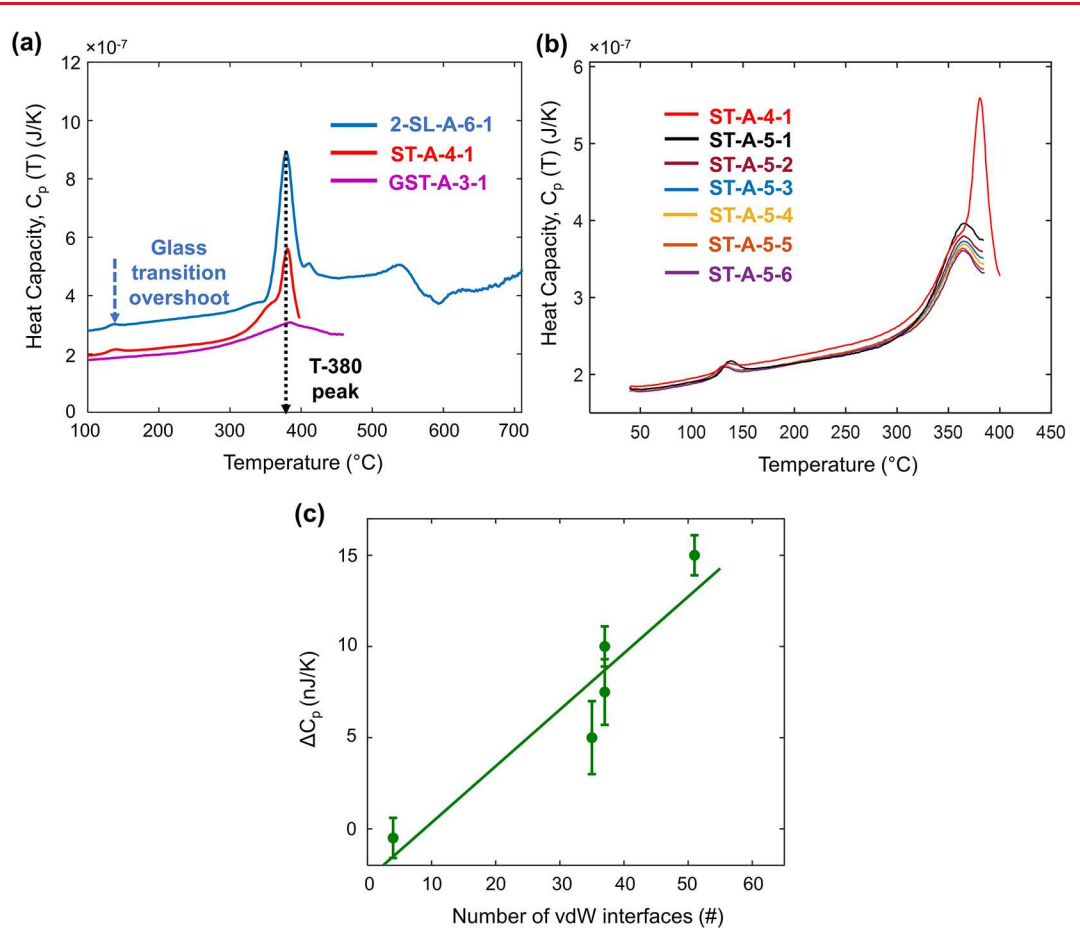


Figure 4. (a) C_p vs T scanning of 32 nm thick ST (red curve, ST-A-4-1) and 28.8 nm thick GST (purple curve, GST-A-3-1) with a 4 nm thick ST as the seed layer. Both ST and GST samples are deposited following the same deposition recipe used for the SL sublayers in this work. Scan 2-SL-A-6-1 (2/1.8 nm/nm ST/GST SL) is also included for comparison. (b) Scan ST-A-4-1 and subsequent scans ST-A-5- N_2 (N_2 = 1-6) of a 32 nm thick ST film. (c) Measured glass transition step height ΔC_p as a function of the number of vdW interfaces for five samples studied in this work. ΔC_p is measured on the first scan with a $T_{\rm max}$ of >200 °C for each sample, including scans 2-SL-A-2-1, 16-SL-A-2-1, 16-SL-B-2-1, ST-A-2-1, and GST-A-2-1.

for SL samples scraped from substrates using conventional calorimetry, but no quantitative enthalpy information has been reported to date.³⁹

In the fourth temperature zone ($T > 550~^{\circ}\text{C}$), we expect to observe pronounced endothermic melting transitions of ST and GST sublayers (denoted as T-bulk) at $\sim 600~^{\circ}\text{C}.^{28-31}$ However, no such transition is detected in the conditioned SL samples during the first scan up to a T_{max} of 710 °C. As shown in Figure 3c, the 2/1.8 nm/nm ST/GST SL (2-SL-A-6-1, blue curve) shows a minimal endothermic signal in this temperature range while the 16/14.4 nm/nm ST/GST SL (16-SL-B-3-1, red curve) shows only two minor peaks. We infer that most of the SL material exists in the metastable state and melts during the T-380 and/or T-shoulder transitions, while there is a minimal amount of thermodynamically stable phases that exhibit bulk melting.

However, the ratio of the metastable and the stable phases can be reversed by applying multiple scans of SLs up to 710 °C, during which samples repeatedly melt and then recrystallize. Figure S5 illustrates such evolution of the 16-SL-B SL, where the T-380 peak progressively decreases and T-bulk gradually increases accordingly. The final scan [16-SL-B-4-100 (green curve in Figure 3c)] shows only a strong peak at 630 °C with a $\Delta H_{\rm m}$ of 95 μ J, which is close to the expected $\Delta H_{\rm m}$ (100 μ J) of the 65 nm SL, as detailed in section IV of the

Supporting Information. We believe that SL transforms from a metastable state to a stable bulk-like state with the material amount approximately conserved as indicated in section III of the Supporting Information. It is noted that the T-glass feature also disappears after such $T_{\rm max}$ = 710 °C scans. This process is further studied by TEM directly on a NanoDSC sensor 40 as detailed in section VIII of the Supporting Information.

To further understand the origin of T-380 in the SL, it is compared to its homogeneous sublayer counterparts, ST and GST. Their deposition follows the same recipe as that of the SL, including the 4 nm ST seed layer. All ST and GST samples were conditioned (prepulsed up to 250–350 °C) to start with (same as for the SLs). The follow-up scans with $T_{\rm max}$ values of >400 °C for ST-A (ST-A-4-1, red curve) and GST-A (GST-A-3-1, purple curve) are shown in Figure 4a.

Surprisingly, we find that ST-A (32 nm ${\rm Sb_2Te_3}$ with a 4 nm ${\rm Sb_2Te_3}$ seed layer) shows strong repeatable signals of both T-glass and T-380 transitions, which share temperatures similar to those of SLs (Figure 4a). Such a sharp endothermic peak at \sim 400 °C is also revealed by conventional calorimetry on ST nanoflakes $^{41-43}$ and bulk ${\rm ST}^{30}$ (summarized in section IX of the Supporting Information), and its origin is attributed to the premelting of ST.

However, only a small T-380 transition is observed in GST-A (28.8 nm GST with a 4 nm Sb₂Te₃ seed layer) with no

Nano Letters pubs.acs.org/NanoLett Letter

measurable (\sim 1 nJ/K sensitivity of NanoDSC²⁸) T-glass transition. We attribute the presence of this small *T*-380 feature in GST-A to the 4 nm ST seed because GST alone does not exhibit any endothermic signal at \sim 400 °C as displayed in Figure 2b.

We further note that the main difference between ST-A and GST-A is that FCC GST does not have long-range vdW interfaces that are inherent in ST stacks.⁴⁴ Therefore, for all samples in this work, we correlate glass transition step height ΔC_{ν} (measured by the first scan to $T_{\rm max}$ < 200 °C) with the number of vdW interfaces (including both homogeneous ST/ ST and heterogeneous ST/GST SL types), as shown in Figure 4c. We find that the strength of the glass transition progressively increases with the number of interfaces. It suggests that vdW interfaces within the SLs could be a promoter of the Te-rich glassy structure inherent in the stacked SL layers. On the basis of the comparisons described above, we conclude that in the SLs, ST sublayers play critical roles in promoting not only the vdW interfaces but also the T-380 and glass transitions of these SLs, which could be responsible for their low-power switching operation in PCM devices.

We further discuss the mechanism of the T-380 melting transition, which is probably associated with the vdW interfaces inherent in both the ST and ST/GST SL stacks. A high density of vdW interfaces and grain boundaries may facilitate the formation of metastable phases and could be critical for the T-380 transitions. Additionally, exothermic intermixing between the ST and GST sublayers could also participate in the T-380 transition with a minor enthalpy contribution (see section X of the Supporting Information). In the end, other thin film phenomena, including size-dependent melting, may also contribute to T-380 and reduce the material melting temperature below its bulk value (see section XI of the Supporting Information). The cross-sectional TEM image of the SL on the NanoDSC sensor would provide key information to identify the metastable phase of T-380. However, because of the fragility of the 100 nm SiN_x membrane, so far we have not obtained a satisfactory cross-sectional TEM sample from NanoDSC sensors, and we will keep pushing our effort in this direction.

In summary, using nanocalorimetry in Sb₂Te₃/GST superlattices, we uncovered an endothermic melting transition at \sim 380 °C (T-380) with an \sim 240 °C decrease in temperature and an ~8-fold decrease in enthalpy compared to those of the melting of GST, providing key thermodynamic insights and an original explanation of the increased endurance and low-power consumption of SL-based PCM devices. We propose that the major transition in T-380 is a crystalline-to-liquid melting transition, where other processes, including intermixing between the ST and GST sublayers could, also participate with a minor enthalpy contribution. We also uncovered a rich landscape of phase transitions, including a glass transition (Tglass), endothermic melting (T-380 and T-bulk), and exothermic effects (T-exo) in such superlattices. T-Glass suggests the presence of Te-rich glassy phases in our superlattices, which crystallized during the subsequent scans featuring an exothermic *T*-exo signal. As a result, the crystalline Te-rich phases could be one of the key factors for the remarkably strong and repeatable T-380 transition. Hightemperature scanning of the superlattice converts its T-380 transition into *T*-bulk, expected from the phase diagram. These findings further show that NanoDSC is a powerful tool for

improving our understanding of superlattices for energyefficient data storage and computing.

ASSOCIATED CONTENT

Supporting Information

The Supporting Information is available free of charge at https://pubs.acs.org/doi/10.1021/acs.nanolett.3c01049.

Bar plots for pulsing parameters and sequences in this work (section I), justification for the crystalline-to-liquid melting transition in T-380 (section II), modeling the reduced transition enthalpy for SL based on Hess' law (section III), calculation of the expected $C_p(100 \, ^{\circ}\text{C})$ for a 65 nm 2/1.8 nm/nm ST/GST SL (section IV), quantitative analysis of the glass transition and exothermic transition for scans 2-SL-A-2-1 and 2-SL-A-3-1 (section V), glass transition overshoot in a series with multiple scans (section VI), high-temperature scans for 16-SL-B (section VII), TEM results for sample 16-SL-B (section VIII), summary of previous calorimetry research (T > 300 °C) on Sb₂Te₃ (section IX), modeling the heat of intermixing/reaction between ST and GST sublayers in a 65 nm SL (section X), and role of Te-rich phases in T-380 (section XI) (PDF)

AUTHOR INFORMATION

Corresponding Author

Leslie H. Allen — Department of Materials Science and Engineering, Coordinated Science Laboratory and Frederick-Seitz Materials Research Laboratory, University of Illinois at Urbana-Champaign, Urbana, Illinois 61801, United States; orcid.org/0000-0001-9323-3767; Phone: (217) 333-7918; Email: L-ALLEN9@illinois.edu

Authors

Jie Zhao – Department of Materials Science and Engineering, Coordinated Science Laboratory and Frederick-Seitz Materials Research Laboratory, University of Illinois at Urbana-Champaign, Urbana, Illinois 61801, United States

Asir Intisar Khan — Department of Electrical Engineering, Stanford University, Stanford, California 94305, United States; orcid.org/0000-0003-4635-4667

Mikhail Y. Efremov – College of Engineering, University of Wisconsin—Madison, Madison, Wisconsin 53706, United States; orcid.org/0000-0002-6379-9433

Zichao Ye — Department of Materials Science and Engineering, Coordinated Science Laboratory and Frederick-Seitz Materials Research Laboratory, University of Illinois at Urbana-Champaign, Urbana, Illinois 61801, United States

Xiangjin Wu – Department of Electrical Engineering, Stanford University, Stanford, California 94305, United States

Kangsik Kim – Center for Multidimensional Carbon Materials, Institute for Basic Science (IBS), Ulsan 44919, Republic of Korea

Zonghoon Lee — Center for Multidimensional Carbon Materials, Institute for Basic Science (IBS), Ulsan 44919, Republic of Korea; Department of Materials Science and Engineering, Ulsan National Institute of Science and Technology (UNIST), Ulsan 44919, Republic of Korea; orcid.org/0000-0003-3246-4072

H.-S. Philip Wong — Department of Electrical Engineering, Stanford University, Stanford, California 94305, United States Eric Pop — Department of Electrical Engineering, Stanford University, Stanford, California 94305, United States; Department of Materials Science and Engineering, Stanford University, Stanford, California 94305, United States; orcid.org/0000-0003-0436-8534

Complete contact information is available at: https://pubs.acs.org/10.1021/acs.nanolett.3c01049

Author Contributions

^VJ.Z. and A.I.K. contributed equally to this work.

Author Contributions

A.I.K. and J.Z. conceived the idea. J.Z. and A.I.K. designed the experiments. A.I.K. performed the deposition of the samples with help from X.W. Z.Y. fabricated the sensors. M.Y.E. fabricated the NanoDSC system. J.Z. calibrated the sensors and performed the nanocalorimetry measurements (with input from Z.Y. and L.H.A.). J.Z. analyzed the data (with input from L.H.A., Z.Y., A.I.K., and M.Y.E.). K.K. and Z.L. performed high-resolution STEM. M.Y.E., J.Z., A.I.K., and L.H.A. wrote the manuscript with input from Z.Y. All authors discussed the results and edited the manuscript.

Notes

The authors declare no competing financial interest.

ACKNOWLEDGMENTS

J.Z. and L.H.A. acknowledge the financial support by National Science Foundation Grants DMR-1409953 and DMR-1809573. The NanoDSC sensors were fabricated at the Cornell Nanoscale Facility (Project #522-94), a member of the National Nanotechnology Infrastructure Network (NNIN). E.P., A.I.K., and X.W. acknowledge the financial support from the Semiconductor Research Corporation (SRC) and the member companies of the Stanford Non-Volatile Memory Technology Research Initiative (NMTRI). A.I.K. also acknowledges support from Stanford Graduate Fellowship. Materials characterization was carried out in part in the Frederick Seitz Materials Research Laboratory, University of Illinois at Urbana-Champaign. This work was also supported by the Institute for Basic Science (IBS-R091-G1).

REFERENCES

- (1) Wong, H.-S. P.; Raoux, S.; Kim, S.; Liang, J.; Reifenberg, J. P.; Rajendran, B.; Asheghi, M.; Goodson, K. E. Phase Change Memory. *Proceedings of the IEEE* **2010**, *98*, 2201–2227.
- (2) Ovshinsky, S. R. Reversible Electrical Switching Phenomena in Disordered Structures. *Phys. Rev. Lett.* **1968**, *21*, 1450.
- (3) Mittal, S.; Vetter, J. S. A Survey of Software Techniques for Using Non-Volatile Memories for Storage and Main Memory Systems. *IEEE Transactions on Parallel and Distributed Systems* **2016**, 27, 1537–1550.
- (4) Wuttig, M.; Yamada, N. Phase-Change Materials for Rewriteable Data Storage. *Nature materials* **2007**, *6*, 824–832.
- (5) Raoux, S.; Xiong, F.; Wuttig, M.; Pop, E. Phase Change Materials and Phase Change Memory. MRS Bull. 2014, 39, 703–710.
- (6) Sebastian, A.; Le Gallo, M.; Burr, G. W.; Kim, S.; BrightSky, M.; Eleftheriou, E. Tutorial: Brain-Inspired Computing Using Phase-Change Memory Devices. *J. Appl. Phys.* **2018**, *124*, 111101.
- (7) Sebastian, A.; Le Gallo, M.; Khaddam-Aljameh, R.; Eleftheriou, E. Memory Devices and Applications for in-Memory Computing. *Nature Nanotechnol.* **2020**, *15*, 529–544.
- (8) Kuzum, D.; Jeyasingh, R. G.; Lee, B.; Wong, H.-S. P. Nanoelectronic Programmable Synapses Based on Phase Change Materials for Brain-Inspired Computing. *Nano Lett.* **2012**, *12*, 2179–2186.

- (9) Khan, A. I.; Kwon, H.; Islam, R.; Perez, C.; Chen, M. E.; Asheghi, M.; Goodson, K. E.; Wong, H.-S. P.; Pop, E. Two-Fold Reduction of Switching Current Density in Phase Change Memory Using Bi₂Te₃ Thermoelectric Interfacial Layer. *IEEE Electron Device Lett.* **2020**, *41*, 1657–1660.
- (10) Khan, A. I.; Wu, X.; Perez, C.; Won, B.; Kim, K.; Ramesh, P.; Kwon, H.; Tung, M. C.; Lee, Z.; Oh, I.-K.; et al. Unveiling the Effect of Superlattice Interfaces and Intermixing on Phase Change Memory Performance. *Nano Lett.* **2022**, *22*, 6285–6291.
- (11) Simpson, R. E.; Fons, P.; Kolobov, A. V.; Fukaya, T.; Krbal, M.; Yagi, T.; Tominaga, J. Interfacial Phase-Change Memory. *Nature Nanotechnol.* **2011**, *6*, 501–505.
- (12) Khan, A. I.; Kwon, H.; Chen, M. E.; Asheghi, M.; Wong, H.-S. P.; Goodson, K. E.; Pop, E. Electro-Thermal Confinement Enables Improved Superlattice Phase Change Memory. *IEEE Electron Device Lett.* **2022**, *43*, 204–207.
- (13) Khan, A. I.; Daus, A.; Islam, R.; Neilson, K. M.; Lee, H. R.; Wong, H.-S. P.; Pop, E. Ultralow–Switching Current Density Multilevel Phase-Change Memory on a Flexible Substrate. *Science* **2021**, *373*, 1243–1247.
- (14) Ding, K.; Wang, J.; Zhou, Y.; Tian, H.; Lu, L.; Mazzarello, R.; Jia, C.; Zhang, W.; Rao, F.; Ma, E. Phase-Change Heterostructure Enables Ultralow Noise and Drift for Memory Operation. *Science* **2019**, *366*, 210–215.
- (15) Kolobov, A. V.; Fons, P.; Saito, Y.; Tominaga, J. Atomic Reconfiguration of Van Der Waals Gaps as the Key to Switching in GeTe/Sb₂Te₃ Superlattices. *ACS omega* **2017**, *2*, 6223–6232.
- (16) Boniardi, M.; Boschker, J. E.; Momand, J.; Kooi, B. J.; Redaelli, A.; Calarco, R. Evidence for Thermal-Based Transition in Super-Lattice Phase Change Memory. *Phys. Status Solidi RRL* **2019**, *13*, 1800634.
- (17) Térébénec, D.; Castellani, N.; Bernier, N.; Sever, V.; Kowalczyk, P.; Bernard, M.; Cyrille, M.-C.; Tran, N.-P.; Hippert, F.; Noé, P. Improvement of Phase-Change Memory Performance by Means of GeTe/Sb₂Te₃ Superlattices. *Phys. Status Solidi RRL* **2021**, 15, 2000538.
- (18) Shen, J.; Lv, S.; Chen, X.; Li, T.; Zhang, S.; Song, Z.; Zhu, M. Thermal Barrier Phase Change Memory. ACS Appl. Mater. Interfaces 2019, 11, 5336–5343.
- (19) Kwon, H.; Khan, A. I.; Perez, C.; Asheghi, M.; Pop, E.; Goodson, K. E. Uncovering Thermal and Electrical Properties of Sb₂Te₃/GeTe Superlattice Films. *Nano Lett.* **2021**, *21*, 5984–5990.
- (20) Lai, S.; Ramanath, G.; Allen, L.; Infante, P.; Ma, Z. High-Speed (104 C/S) Scanning Microcalorimetry with Monolayer Sensitivity (J/M2). *Applied physics letters* **1995**, *67*, 1229–1231.
- (21) Olson, E. A.; Efremov, M. Y.; Zhang, M.; Zhang, Z.; Allen, L. H. The Design and Operation of a Mems Differential Scanning Nanocalorimeter for High-Speed Heat Capacity Measurements of Ultrathin Films. *J. Microelectromech. Syst.* **2003**, *12*, 355–364.
- (22) Efremov, M. Y.; Olson, E. A.; Zhang, M.; Schiettekatte, F.; Zhang, Z.; Allen, L. H. Ultrasensitive, Fast, Thin-Film Differential Scanning Calorimeter. *Review of scientific instruments* **2004**, *75*, 179–191.
- (23) Efremov, M. Y.; Olson, E.; Zhang, M.; Lai, S.; Schiettekatte, F.; Zhang, Z.; Allen, L. Thin-Film Differential Scanning Nanocalorimetry: Heat Capacity Analysis. *Thermochimica acta* **2004**, *412*, 13–23.
- (24) Yi, F.; LaVan, D. A. Nanocalorimetry: Exploring Materials Faster and Smaller. *Applied Physics Reviews* **2019**, *6*, 031302.
- (25) Nozard, H.; Schiettekatte, F. Arrhenius Behavior of Crystallization at up to 184 000 K/S in Ge₂Sb₂Te₅ Thin Films. *AIP Advances* **2021**, *11*, 085226.
- (26) Hu, L.; Zhang, Z.; Zhang, M.; Efremov, M. Y.; Olson, E. A.; de la Rama, L. P.; Kummamuru, R. K.; Allen, L. H. Self-Assembly and Ripening of Polymeric Silver— Alkanethiolate Crystals on Inert Surfaces. *Langmuir* **2009**, 25, 9585—9595.
- (27) Kummamuru, R. K.; Hu, L.; Cook, L.; Efremov, M. Y.; Olson, E. A.; Allen, L. H. A Close Proximity Self-Aligned Shadow Mask for Sputter Deposition onto a Membrane or Cavity. *Journal of Micromechanics and Microengineering* **2008**, *18*, 095027.

Nano Letters pubs.acs.org/NanoLett Letter

- (28) Zhao, J.; Hui, J.; Ye, Z.; Lai, T.; Efremov, M. Y.; Wang, H.; Allen, L. H. Exploring "No Man's Land" — Arrhenius Crystallization of Thin-Film Phase Change Material at 1 000 000 K S⁻¹ Via Nanocalorimetry. Advanced Materials Interfaces 2022, 9, 2200429.
- (29) Kalb, J. A. Crystallization Kinetics in Antimony and Tellurium Alloys Used for Phase Change Recording. Aachen, Techn. Hochsch., Diss. 2006, 2006, n/a.
- (30) Legendre, B.; Feutelais, Y.; Didry, J. Capacite Calorifique Molaire Du Compose Sb_{0.405} Te_{0.595} Dans Les Etats Solides Et Liquides Entre 298 K Et 922 K. J. Therm. Anal. Calorim. 1988, 34,
- (31) Howlett, B.; Bever, M.; Misra, S. On Thermodynamic Properties of Compounds Sb₂Se₃ Sb₂Te₃+ Bi₂Te₃. Metall. Trans. 1964, 230, 1367.
- (32) Rycerz, L. Practical Remarks Concerning Phase Diagrams Determination on the Basis of Differential Scanning Calorimetry Measurements. J. Therm. Anal. Calorim. 2013, 113, 231-238.
- (33) Barrow, G. M. Physical Chemistry, 3rd ed.; McGraw-Hill: New York, 1973; pp 135-157.
- (34) Seyler, R. J. Assignment of the Glass Transition; ASTM International, 1994; Vol. 1249.
- (35) Rocca, J.; Erazú, M.; Fontana, M.; Arcondo, B. Crystallization Process on Amorphous GeTeSb Samples near to Eutectic Point Ge₁₅Te₈₅. J. Non-Cryst. Solids **2009**, 355, 2068–2073.
- (36) Efremov, M. Y.; Olson, E. A.; Zhang, M.; Zhang, Z.; Allen, L. H. Glass Transition in Ultrathin Polymer Films: Calorimetric Study. Phys. Rev. Lett. 2003, 91, 085703.
- (37) Wunderlich, B. The Nature of the Glass Transition and Its Determination by Thermal Analysis; ASTM Special Technical Publication; ASTM International, 1994; Vol. 1249, p 17.
- (38) Legendre, B.; Hancheng, C.; Bordas, S.; Clavaguera-Mora, M. Phase Diagram of the Ternary System Ge-Sb-Te. I. The Subternary GeTe- Sb₂Te₃-Te. Thermochim. Acta 1984, 78, 141-157.
- (39) Tominaga, J.; Fons, P.; Kolobov, A.; Shima, T.; Chong, T. C.; Zhao, R.; Lee, H. K.; Shi, L. Role of Ge Switch in Phase Transition: Approach Using Atomically Controlled GeTe/Sb₂Te₃ Superlattice. Japanese journal of applied physics 2008, 47, 5763.
- (40) Zhang, M.; Olson, E.; Twesten, R.; Wen, J.; Allen, L.; Robertson, I.; Petrov, I. In Situ Transmission Electron Microscopy Studies Enabled by Microelectromechanical System Technology. Journal of materials research 2005, 20, 1802-1807.
- (41) Sun, S.; Peng, J.; Jin, R.; Song, S.; Zhu, P.; Xing, Y. Template-Free Solvothermal Synthesis and Enhanced Thermoelectric Performance of Sb₂Te₃ Nanosheets. Journal of alloys and compounds 2013, 558, 6-10.
- (42) Dong, G.-H.; Zhu, Y.-J.; Cheng, G.-F.; Ruan, Y.-J. Sb₂Te₃ Nanobelts and Nanosheets: Hydrothermal Synthesis, Morphology Evolution and Thermoelectric Properties. Journal of alloys and compounds 2013, 550, 164-168.
- (43) Schulz, S.; Heimann, S.; Friedrich, J.; Engenhorst, M.; Schierning, G.; Assenmacher, W. Synthesis of Hexagonal Sb₂Te₃ Nanoplates by Thermal Decomposition of the Single-Source Precursor (Et₂Sb)₂Te. Chem. Mater. 2012, 24, 2228-2234.
- (44) Zhang, B.; Wang, X.-P.; Shen, Z.-J.; Li, X.-B.; Wang, C.-S.; Chen, Y.-J.; Li, J.-X.; Zhang, J.-X.; Zhang, Z.; Zhang, S.-B.; Han, X.-D. Vacancy Structures and Melting Behavior in Rock-Salt GeSbTe. Sci. Rep. 2016, 6, 25453.

□ Recommended by ACS

Direct Visualization of Subnanometer Variations in the Excitonic Spectra of 2D/3D Semiconductor/Metal Heterostructures

Kate Reidy, Juan Carlos Idrobo, et al.

JANUARY 13, 2023 NANO I FTTERS

RFAD 🗹

On-Chip Time-Domain Terahertz Spectroscopy of Superconducting Films below the Diffraction Limit

Alex M. Potts, Andrea F. Young, et al.

MAY 01, 2023

NANO LETTERS

READ **C**

Bend-Induced Ferroelectric Domain Walls in α-In,Se₃

Edmund Han, Pinshane Y. Huang, et al.

APRIL 14, 2023

ACS NANO

READ **C**

Real-Time Measure of the Lattice Temperature of a Semiconductor Heterostructure Laser via an On-Chip **Integrated Graphene Thermometer**

Leonardo Viti, Miriam S. Vitiello, et al.

MARCH 08, 2023

ACS NANO

READ **C**

Get More Suggestions >